

Lawrence Berkeley National Laboratory

Energy Storage & Distributed Resources

Title

Three-Tier Hierarchical Structures for Extreme Pool Boiling Heat Transfer Performance

Permalink

<https://escholarship.org/uc/item/9054k21g>

Journal

Advanced Materials, 34(32)

ISSN

0935-9648

Authors

Song, Youngsup
Díaz-Marín, Carlos D
Zhang, Lenan
[et al.](#)

Publication Date

2022-08-01

DOI

10.1002/adma.202200899

Copyright Information

This work is made available under the terms of a Creative Commons Attribution-NonCommercial License, available at <https://creativecommons.org/licenses/by-nc/4.0/>

Peer reviewed

1 **Three-Tier Hierarchical Structures for Extreme Pool Boiling Heat Transfer**
2 **Performance**

3
4 *Youngsup Song, Carlos D. Díaz-Marín, Lenan Zhang, Hyeongyun Cha, Yajing Zhao, and*
5 *Evelyn N. Wang**

6
7
8 Dr. Y. Song, C. D. Díaz-Marín, L. Zhang, Dr. H. Cha, Y. Zhao, Prof. E. N. Wang
9 Department of Mechanical Engineering, Massachusetts Institute of Technology, Cambridge,
10 MA 02139, USA
11 E-mail: enwang@mit.edu

12
13 **Keywords:** Hierarchical structure, Microstructure, Nanostructure, Critical heat flux, Heat
14 transfer coefficient, Phase change heat transfer
15

16 Boiling is an effective energy transfer process with substantial utility in energy applications.
17 Boiling performance is described mainly by the heat transfer coefficient (HTC) and critical
18 heat flux (CHF). Recent efforts for the simultaneous enhancement of HTC and CHF have
19 been limited by an intrinsic trade-off between them — HTC enhancement requires high
20 nucleation site density, which can increase bubble coalescence resulting in limited CHF
21 enhancement. In this work, we overcome this trade-off by designing three-tier hierarchical
22 structures. We minimize bubble coalescence to enhance CHF by defining nucleation sites with
23 microcavities interspersed within hemi-wicking structures. Meanwhile, the reduced nucleation
24 site density is compensated for by incorporating nanostructures that promote evaporation for
25 HTC enhancement. Our hierarchical structures demonstrate the simultaneous enhancement of
26 HTC and CHF up to 389% and 138%, respectively, compared to a smooth surface. This
27 extreme boiling performance can lead to significant energy savings in a variety of boiling
28 applications.

29
30 The global demand for electrical power has been continuously growing ~3% annually during
31 the past decade.^[1] Over 90% of this electrical power is generated by steam turbines,^[2] where
32 boiling generates the steam. Steam generation is also essential in sustainability such as for

1 food and chemical processing, water purification, sterilization, and harvesting.^[3] Furthermore,
2 the high heat dissipation capability of boiling enables such processes for thermal management
3 of high flux energy applications such as concentrated photovoltaics, fast-charging batteries,
4 data centers, and integrated electronics.^[4] The continuing growth in energy demands puts an
5 increased emphasis on achieving even larger enhancements in boiling performance.

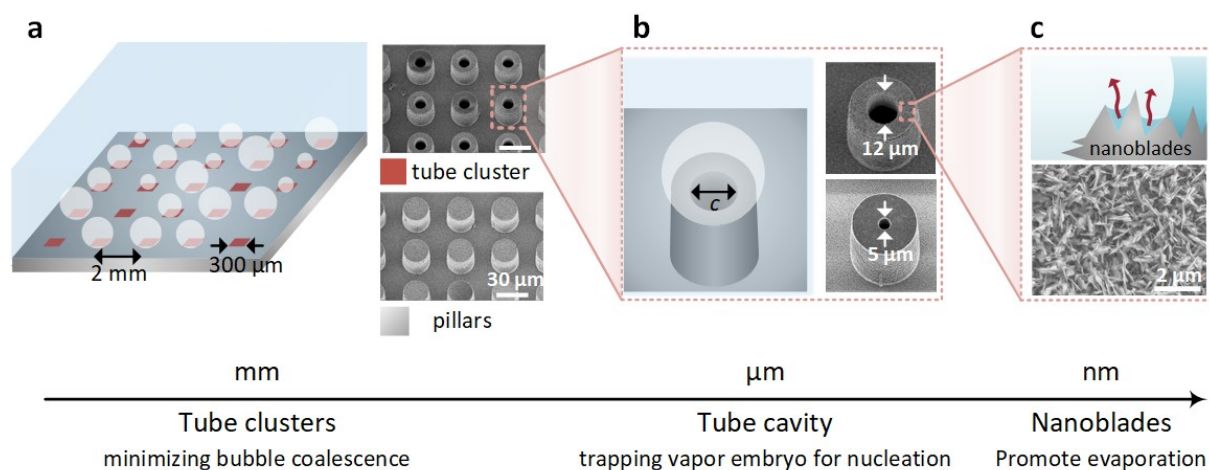
6 The heat transfer coefficient (HTC, h) and critical heat flux (CHF, q_{CHF}) are two
7 major parameters that quantify boiling performance. The HTC describes the efficiency of
8 boiling heat transfer, defined as the ratio of heat flux (q) to the wall superheat (ΔT_w), i.e.,
9 $h = q / \Delta T_w$. Here ΔT_w is the temperature difference between the boiling
10 surface and the saturated liquid. In the nucleate boiling regime, the heat flux increases with
11 the wall superheat. However, when the heat flux is sufficiently high, excessive vapor bubbles
12 nucleated on the boiling surface prevent the liquid from rewetting the surface and, in turn,
13 form an insulating vapor film over the surface. This vapor film becomes a thermal barrier that
14 leads to a drastic increase in wall superheat and burnout of a boiling system. This transition
15 from nucleate boiling to film boiling is known as the boiling crisis, where the maximum heat
16 flux is CHF. Enhancing CHF, therefore, can either enable larger safety margins or extend the
17 operational heat flux range for boiling systems.^[5]

18 Recent efforts to enhance boiling heat transfer have focused on engineering the working fluid
19 or surface properties.^[6] In particular, engineering surface structures has received greater
20 attention owing to the constraints on chemical compatibility or operational conditions which
21 can limit the choice of the working fluid. Representative examples of surface structures that
22 effectively enhance CHF are known to be hemi-wicking surfaces such as micropillars and
23 nanowires.^[7] These structures enhance CHF by harnessing thin-film evaporation around
24 pillars and capillary-fed wicking through the structures.^[8] Surfaces with microcavities, on the
25 other hand, have shown improved HTC by trapping vapor embryos that promote nucleation.^[9]

1 Recently, a combination of microtube and micropillar structures, referred to as tube-clusters
2 in pillars (TIP), has shown the ability to tune the HTC and CHF by controlling bubble
3 coalescence while maintaining capillary wicking.^[10] Despite the controllability, achieving
4 extreme enhancement of HTC and CHF simultaneously remains challenging due to the
5 intrinsic trade-off between HTC and CHF associated with nucleation site density. For
6 example, high nucleation site density may increase HTC but decrease CHF because extensive
7 bubble coalescence hinders the capillary wicking performance, while the reduced number of
8 nucleation sites will limit the HTC enhancement. In addition, certain copper-based engineered
9 surfaces have shown simultaneous enhancements of HTC and CHF,^[11] but the change in
10 surface morphology and chemical composition of copper surfaces by in situ oxidation during
11 boiling has made the enhancement mechanism unclear.^[12]

12 In this work, we overcome this trade-off and demonstrate an approach to achieve
13 simultaneous extreme enhancement of HTC and CHF based on chemically stable SiO₂
14 surfaces. By designing a three-tier hierarchically structured TIP surface (h-TIP), we can
15 control vapor nucleation at multiple length scales while providing capillary wicking (**Figure**
16 **1**). For CHF enhancement, we minimized bubble coalescence and exploited capillary wicking
17 by defining separated nucleation sites with tube clusters (shaded dark-red area in Figure 1a).
18 For HTC enhancement, on the other hand, we promoted vapor nucleation with microscale
19 cavities (Figure 1b), where evaporation could be further enhanced by extending the liquid-
20 vapor interfaces on nanostructures (Figure 1c). Our strategy to enhance HTC does not have
21 the detrimental effect of continuing to increase the nucleation site density and as a result,
22 prevents the liquid rewetting process.

23



1
2 **Figure 1.** Schematics and scanning electron microscopy (SEM) images of a hierarchically
3 structured TIP surface (h-TIP) that exhibits capillary wicking while controlling vapor
4 nucleation using multiple length scales. (a) The h-TIP surface consists of hierarchical tube
5 clusters interspersed in hierarchical pillar arrays. Left panel: 2 mm pitch between the tube
6 clusters separates bubbles and minimizes bubble coalescence. The dark-red patterned regions
7 represent the hierarchical tube clusters whereas the grey region is covered by hierarchical
8 pillar structures. Right panel: SEM images of the hierarchical tube structures (top) and
9 hierarchical pillar structures (bottom). Scale bars are 30 μm . (b) Microscale cavity at the
10 center of tube structure traps vapor embryo and promotes nucleation. Left panel: schematic of
11 bubble nucleation on the top of a tube structure. Right panel: SEM images of a hierarchical
12 tube with a cavity diameter of 12 μm (top) and 5 μm (bottom). (c) Nanoblades on top of
13 microstructures augment liquid evaporation under the bubbles. Top panel: schematic of the
14 extended liquid-vapor interface on the nanostructures. Bottom panel: SEM image of the
15 nanostructures created all over the h-TIP and h-Tube surfaces including their tubes, pillars,
16 and flat base.

17

18 We fabricated hierarchically structured TIP surfaces (h-TIP) along with uniform arrays of
19 hierarchically structured tubes (h-Tube), which consist of only tubes, to investigate the

1 effectiveness of bubble separation by TIP structures in the presence of nanostructures. First,
2 microscale structures were created through photolithography and deep-reactive ion etching
3 processes on silicon wafers. The outer diameter, height, and pitch of microtubes and
4 micropillars were fixed at 22, 30, and 40 μm , respectively. To investigate the effects of cavity
5 size on the onset of nucleate boiling temperature, two cavity diameters of 5 and 12 μm were
6 fabricated (SEM images in Figure 1b) for both h-Tube and h-TIP surfaces. According to the
7 theoretical analysis for active cavity sizes for nucleate boiling,^[13] 5 and 12 μm cavities were
8 chosen to initiate vapor nucleation at 11 $^{\circ}\text{C}$ and 5 $^{\circ}\text{C}$ wall superheat, respectively.^[10] The
9 cluster-to-cluster pitch was set to 2 mm based on the capillary length of water (≈ 2.5 mm)
10 (Figure 1a), which has been found as an optimal distance between nucleation sites for
11 effective separation of vapor bubbles in previous works.^[10, 14] On top of the microstructured
12 surfaces, sharp blade-like cupric oxide (CuO) nanostructures were created by sputtering a 500
13 nm copper layer over the microstructures followed by an oxidation in an alkali solution
14 (NaClO_2 , NaOH , Na_3PO_4 , and deionized water with 3.75:5:10:100 wt.%) at 95 $^{\circ}\text{C}$ for 2
15 minutes (SEM image in Figure 1c).^[15] The structural durability of CuO nanostructures during
16 boiling have been demonstrated in previous studies.^[16] At the end, we deposited a 20 nm
17 silicon dioxide (SiO_2) layer using atomic layer deposition to ensure uniform hydrophilicity
18 along the entire hierarchical structure.

19

20 The pool boiling experiments were performed with saturated high-purity deionized water at
21 atmospheric conditions by applying heat flux through a serpentine platinum (Pt) heater on the
22 backside of each sample. This Pt heater was also used for thermometry based on its linear
23 correlation between electrical resistance and temperature. Prior to boiling, all surfaces were
24 cleaned with solvents followed by an argon plasma to remove organic contaminants.^[17] The

1 bubble dynamics during boiling was captured by a high-speed camera (Phantom v7.1, Vision
2 Research) with up to 4000 frames per second.

3

4 **Figure 2a** shows pool boiling curves, i.e., heat flux as a function of wall superheat, of h-TIP
5 and h-Tube surfaces along with microstructured surfaces with the same microscale
6 dimensions such as micropillars, microtubes, and TIP surfaces from the previous work for
7 comparison.^[10] Each surface is named with its structure and the cavity diameter; for example,
8 h-TIP 12 μm is a h-TIP surface that has 12 μm diameter cavity in each tube clusters. We also
9 plotted HTC as a function of heat flux in Figure 2b. All hierarchical structures showed
10 enhanced HTC and CHF values compared with their microstructure counterparts without
11 nanostructures. For example, h-TIP surfaces significantly enhanced HTC values while
12 maintaining the high CHF of TIP surfaces. Compared with up to 209% enhancement (relative
13 to a flat surface) of maximum HTC (h_{max}) on normal TIP surfaces, h-TIP 5 μm and h-TIP 12
14 μm achieved 289 and 389% enhancement, respectively. At the same time, CHF values of h-
15 TIP 5 μm and h-TIP 12 μm were enhanced 138 and 125%, respectively. In fact, the boiling
16 curves of h-TIP surfaces shifted left of the boiling curves of normal TIP surfaces. This
17 simultaneous enhancement of HTC and CHF on h-TIP structures was achieved because the
18 nanostructures extended the liquid-vapor interface. As a result, this effect promoted
19 evaporation and enhanced HTC. Meanwhile, the nucleation site density was maintained
20 (Figure 2c and 2d) to prevent hindering of the liquid rewetting, which would limit CHF
21 enhancement. We attribute two mechanisms within the nanostructures for promoting
22 evaporation and bubble departure frequency. First, the liquid imbibed in the nanostructures
23 can evaporate quickly under the vapor bubbles because of the nanoscale liquid film thickness
24 (mechanism (1) in Figure 2d). Second, when the nanostructures are filled with vapor, the

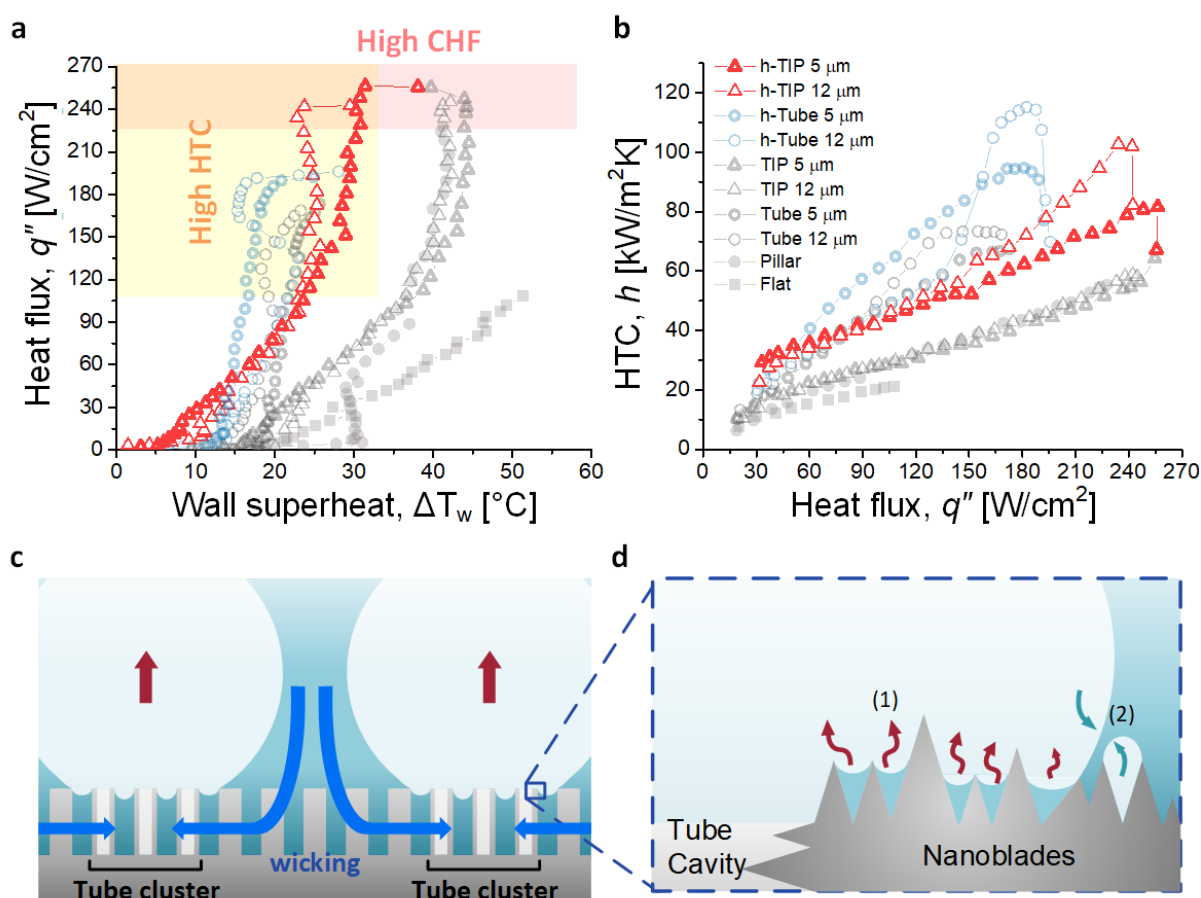
1 vapor can diffuse and merge with a growing bubble above them, which will accelerate the
2 bubble growth and departure frequency (mechanism (2) in Figure 2d).

3 A similar enhancement was observed on h-Tube surfaces compared with normal microtube
4 surfaces due to the enhanced evaporation from the nanostructures. The maximum HTC value
5 of h-Tube 5 μm and h-Tube 12 μm , for example, were 351 and 448% enhancement,
6 respectively. This result is significant improvement compared with the 244% enhancements of
7 h_{max} on normal microtube arrays. In addition to the HTC enhancement, h-Tube surfaces
8 demonstrated higher CHF enhancement than microtube surfaces, where h-Tube 5 μm and h-
9 Tube 12 μm achieved 78 and 82% CHF enhancement, respectively, while Tube 12 μm
10 showed 62% CHF enhancement. Because the extensively high nucleation site density
11 primarily triggered the boiling crises on h-Tube and microtube surfaces, the addition of
12 nanostructures was able to enhance CHF as well as HTC by providing additional evaporation
13 heat flux for a similar nucleation site density near CHF. Yet, the CHF enhancement was still
14 limited compared to TIP and h-TIP surfaces. The pool boiling results of h-TIP and h-Tube
15 surfaces confirm that our h-TIP surfaces maintained the high CHF values of TIP surfaces
16 while significantly improving the HTC because of the effective separation of liquid and vapor
17 paths during boiling, which also allows surfaces to exploit the capillary wicking completely
18 (Figure 2c).

19 Another interesting observation to note was that hierarchical surfaces with 12 μm cavity
20 diameters (h-Tube 12 μm and h-TIP 12 μm) showed a decrease in wall superheat near 20 $^{\circ}\text{C}$
21 while the heat flux increased, a phenomenon known as boiling inversion. However, a similar
22 phenomenon was not observed on hierarchical surfaces with the 5 μm cavity diameter. While
23 previous works attributed the boiling inversion primarily to enhanced macro-convection
24 driven by effective separation of liquid-vapor paths,^[18] another work showed that the boiling
25 inversion disappeared when boiling curves were obtained by decreasing heat flux,^[19] which

1 cannot be explained by the macro-convection hypothesis. Interestingly, our h-TIP 12 μm
 2 surface showed boiling inversion even on the boiling curve obtained by decreasing heat flux.
 3 Understanding the boiling inversion mechanism is still limited and needs further
 4 investigation. A detailed discussion on experimental repeatability and boiling inversion is
 5 available in Section II in the Supporting Information.

6



7

8 **Figure 2.** Pool boiling results and schematics of boiling heat transfer enhancement on h-TIP
 9 surfaces. (a) Pool boiling curves of saturated water on h-Tube and h-TIP surfaces compared
 10 with microstructured surfaces without nanostructures. (b) HTC as a function of heat flux. The
 11 experimental uncertainty is smaller than the marker size. (c) Schematic of the separated
 12 liquid-vapor paths during boiling on an h-TIP surface. Bubbles grow on top of and depart
 13 from tube clusters, while liquids coming outside tube clusters rewet the surface by capillary

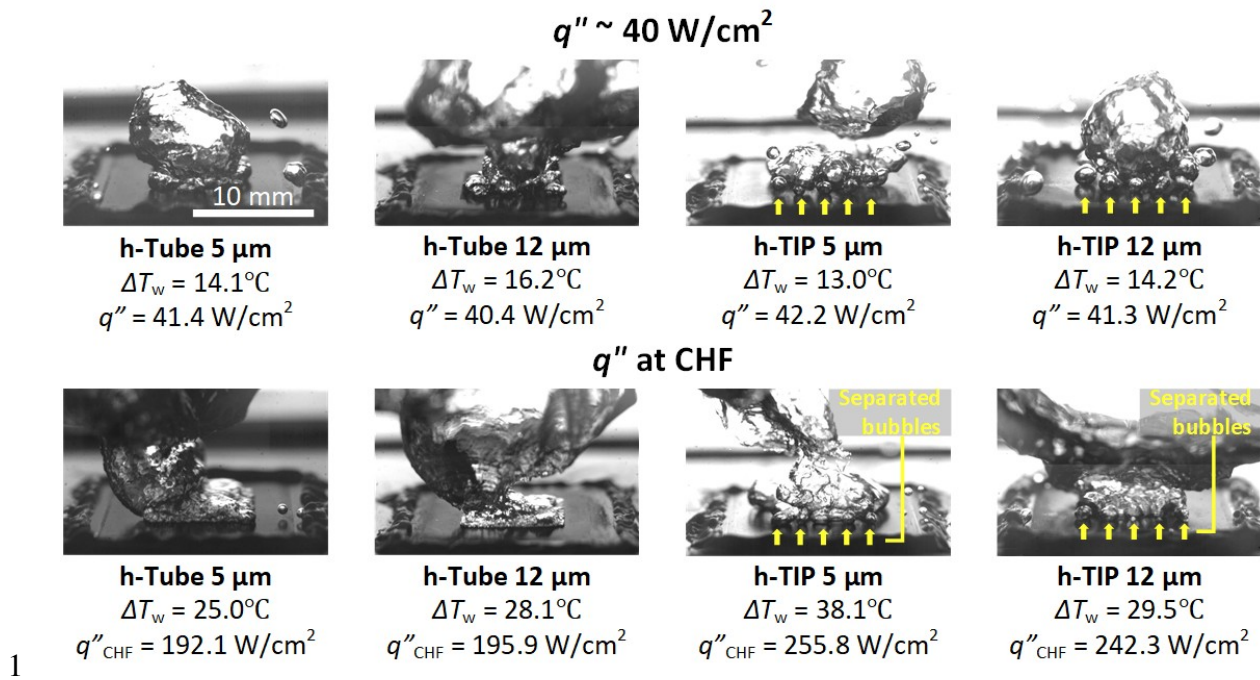
1 wicking. (d) Schematic explaining the two mechanisms for the nanostructure-induced
2 evaporation: (1) rapid evaporation of thin liquid films due to their nanoscale thickness and (2)
3 diffusion of vapor trapped in nanostructures, which accelerates bubble growth and departure.

4

5 We confirmed the different behavior of bubble interactions on h-Tube and h-TIP surfaces by
6 capturing the bubble dynamics with a high-speed camera (Phantom v7.1, Vision Research) up
7 to 4000 frames per second. High-speed movies are available in the Supporting Information.

8 **Figure 3** shows images capturing the bubble dynamics on h-Tube and h-TIP surfaces at a
9 moderate heat flux of $\approx 40 \text{ W cm}^{-2}$ (the first row of Figure 3) and at CHF (the second row of
10 Figure 3). Since microscale cavities promote nucleation, significantly higher nucleation site
11 densities were observed on h-Tube surfaces compared to h-TIP surfaces. Accordingly,
12 bubbles on h-Tube surfaces showed intensive interactions with each other. In the case of h-
13 TIP surfaces, on the contrary, bubbles nucleated from spatially separated tube clusters, which
14 led to a reduced bubble coalescence. This behavior continued until CHF was reached. We
15 observed that vapor films formed over h-Tube surfaces at CHF, which suggests that CHF
16 enhancement was limited because of the high nucleation site density. The separation of
17 nucleating bubbles on h-TIP surfaces, on the other hand, was effective even at CHF; therefore,
18 the CHF on h-TIP surfaces was enhanced until it was limited by capillary wicking. This
19 observation supports our boiling curve analysis that h-TIP surfaces enhanced HTC without
20 increasing the nucleation site density, resulting in simultaneous enhancement of HTC and
21 CHF.

22



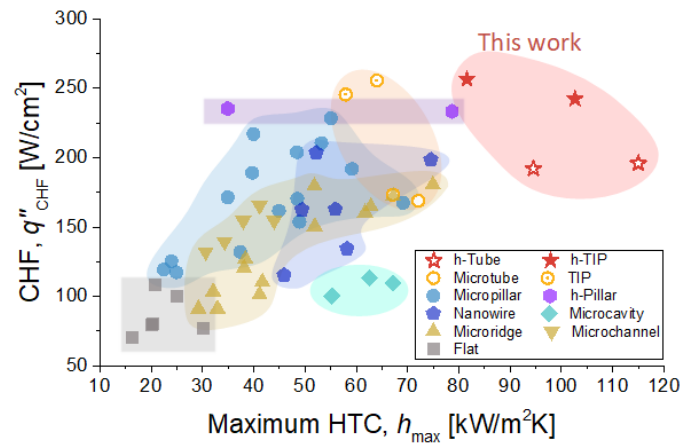
1 **Figure 3.** Images of bubbles on h-Tube and h-TIP surfaces during boiling captured by a high-
 2 speed camera with a 19° tilt angle and up to 4000 frames per second. First and second rows
 3 show bubble dynamics at a heat flux of $\approx 40 \text{ W cm}^{-2}$ and at CHF, respectively. h-TIP surfaces
 4 showed effectively separated bubbles even at CHF (highlighted with yellow arrows), while h-
 5 Tube surfaces showed extensive bubble coalescence which led to the formation of vapor films
 6 at CHF. High-speed movies are available in the Supporting Information.
 7

8

9 In **Figure 4**, we compared CHF (q''_{CHF}) and the maximum HTC (h_{max}) values of h-
 10 TIP and h-Tube surfaces with different micro/nano structures from the literature. The
 11 structures from the literature include microtube and TIP,^[10] micropillar,^[7a, 20] hierarchically
 12 structured pillar (h-Pillar),^[21] nanowire,^[7d, 22] microcavity,^[10, 23] microridge,^[24] and
 13 microchannel.^[23, 25] All data shown in Figure 4 are summarized in Supporting Information
 14 Table S1. Here we compared the data of SiO₂ surfaces, except nanowires based on silicon, to
 15 compare the effects of structures excluding the effects of material properties. Our h-TIP
 16 surfaces showed the highest simultaneous enhancement of HTC and CHF among all other

1 structures, as shown on the top-right corner of the plot. Yet, there are opportunities for further
 2 enhancement of h-TIP surfaces by optimizing microscale structure dimensions such as the
 3 outer diameter, pitch, and height of hierarchical tube and pillars, which were fixed in this
 4 work.

5



6

7 **Figure 4.** Regime map of CHF (q''_{CHF}) and maximum HTC (h_{max}) values of
 8 different SiO_2 micro/nano structures and Si nanowires. This work with h-TIP shows the
 9 highest performance (upper right region) with simultaneous CHF and HTC enhancement.

10

11 In this work, we developed boiling surface structures that achieved superior pool boiling
 12 performance via multi-scale control of vapor nucleation on hemi-wicking surfaces. Our
 13 strategy included the minimization of bubble coalescence, promoting vapor nucleation and
 14 enhancing evaporation by engineering surfaces with separated tube clusters, microscale
 15 cavities, and nanostructures, respectively. Meanwhile, capillary wicking performance was
 16 maintained in the presence of dynamically interacting boiling bubbles. We conducted
 17 saturated pool boiling experiments with water at atmospheric conditions and analyzed the
 18 results, with supporting data from high-speed imaging of bubble dynamics. Our hierarchical
 19 TIP surfaces (h-TIP) achieved significant HTC enhancement up to 389% as well as 138%

1 CHF enhancement compared to a smooth surface. This work provides surface design
2 guidelines for extreme pool boiling heat transfer, that is, the effective separation of nucleating
3 bubbles, enhanced evaporation by nanostructures, and exploiting capillary wicking are
4 essential. We expect that our design guidelines can be adopted for industry-scale boiling
5 applications by creating surfaces using a scalable processes such as sandblasting;^[26] for
6 example, a similar hierarchical structure can be created by sandblasting a surface using first a
7 larger abrasive and subsequently a smaller abrasive. Furthermore, physical insights obtained
8 in this work can be utilized in other applications such as electrochemical oxygen or hydrogen
9 evolution reaction, where surface-bubble interactions play a crucial role in their performance.
10 ^[27] The enhanced boiling performance promises significant energy savings in various boiling
11 applications, including steam power plants, desalination, thermal management of concentrated
12 photovoltaics, etc.

13

14 **Experimental Section**

15 *Surface fabrication:* We first fabricated microscale structures through photolithography and
16 deep-reactive etching processes on silicon wafers that had 1 μm thermal oxide on both sides.
17 A 2 μm layer of photoresist (SPR 700, Microposit) was spin coated with 3600 rpm for 30
18 seconds on one side of the wafers. After prebaking in a box furnace at 95 $^{\circ}\text{C}$ for 45 min, the
19 photoresist was exposed using an MLA150 Maskless Aligner. The resist was then developed
20 in the developer (CD26, Microposit) followed by postbaking at 120 $^{\circ}\text{C}$ for 30 min. The
21 exposed silicon dioxide layer was etched by reactive ion etching (RIE) (Precision 5000,
22 Applied Materials) with CF_4 as a primary gas. Then, micropillars and microtubes were etched
23 in the bulk silicon with deep reactive ion etching (MESC Multiplex ICP, STS) based on SF_6
24 and C_4F_8 . The processed wafers were treated with oxygen plasma in the RIE chamber to
25 remove the C_4F_8 passivation layers and organic contaminants. To create nanostructures over

1 the microfabricated surfaces, we sputtered a 500 nm copper (Cu) layer with a 50 nm titanium
2 (Ti) adhesion layer. The Cu layer was then oxidized in an alkali solution (NaClO₂, NaOH,
3 Na₃PO₄, and deionized water with 3.75:5:10:100 wt.%) at 95 °C for 2 minutes, resulting in
4 sharp blade-like cupric oxide (CuO) nanostructures. Finally, the entire surfaces of hierarchical
5 structures were covered by a 20 nm silicon dioxide (SiO₂) layer using atomic layer deposition.

6
7 *Pool boiling characterization:* The pool boiling setup consisted of a glass chamber with an
8 Ultem fixture at the bottom and a PEEK fixture at the top. The test sample (20 × 20 mm²)
9 attached to an Ultem fixture with adhesive sealant (High-temperature RTV Silicone,
10 Permatex). The test sample was fabricated based on a 650-μm-thick silicon substrate. A rope
11 heater was used to maintain the saturation temperature in the glass chamber by preventing
12 heat loss. At the top PEEK fixture, an immersion heater and a reflux condenser were installed.
13 We first pre-heated de-ionized water in a separate electric kettle before introducing the water
14 into the glass chamber. The immersion heater was used to degas the pre-heated water by
15 boiling for another 30 minutes before experimental measurements. During this degassing
16 period, a heat flux of $\approx 50 \text{ W/cm}^2$ was applied. The reflux condenser condensed water vapor
17 and allowed it to return back to the pool as liquid. A power supply (KLP 600-4-1200, Kepco)
18 provided power for the Joule heater of the 10 × 10 mm² heating area (A_h) defined by the
19 serpentine Pt heater on the back side of the sample through Au/Pt electrodes. A multimeter
20 (2110 5½, Keithley) formed a serial connection with the power supply and the sample for the
21 current measurement across the heater (I), while the other multimeter (34401A, Agilent) was
22 connected in parallel for the voltage-drop measurement (V). The input heat flux was then
23 evaluated as $q = (I \times V) / A_h$. The Pt backside heater also served as a
24 resistance temperature detector (RTD) for temperature characterization. Prior to pool boiling
25 experiments, test samples were placed in a furnace with a high accuracy Pt RTD (Omega

1 Engineering, RTD-810) close to it. The heater resistance was then measured at six different
2 temperature set points. The dwell time at each set point was at least 2 hours to ensure thermal
3 equilibrium within the furnace. The resistance was measured with the four-wire method using
4 a temperature input module (National Instruments, NI-9226 and cDAQ-9171). The
5 experimental data were fit with a linear model. The linear fit was used to convert the measured
6 resistance to the temperature of the heater during pool boiling experiments. Because of the
7 size mismatch between the actual heating area and the exposed surface area, there could be
8 heat loss through the sample thickness. We numerically calibrated (COMSOL Multiphysics
9 5.3a LiveLink for MATLAB) the boiling heat flux and wall superheat based on the measured
10 input heat flux and the heater temperature. In the numerical simulation, we iterated the
11 calculations by changing the heat transfer coefficients at the boiling surface until the
12 calculation of the backside heater temperature matched the experimentally measured
13 temperature. All data points in the boiling curves were calibrated in this manner. Details of
14 the boiling test rig with schematics, experimental procedure, and measurement uncertainty are
15 available in Section I of the Supporting Information.

16

17 **Supporting Information**

18 Supporting Information is available from the Wiley Online Library or from the author.

19

20 **Acknowledgements**

21 Y. Song and H. Cha acknowledge that the information, data, or work presented herein was
22 funded in part by the Advanced Research Projects Agency-Energy (ARPA-E), U. S.
23 Department of Energy, under Award Number DE-AR0000ABC. C. D. Díaz-Marín
24 acknowledges the Air Force Office of Scientific Research under Grant No. FA9550-19-1-0392
25 with Dr. Ali Sayir as program manager, and a Professor Amar G. Bose Research Grant. L.
26 Zhang acknowledges the Singapore-MIT Alliance for Research and Technology (SMART)
27 program. This work was carried out in part through the use of MIT.nano's facilities. This work
28 was carried out in part through the use of MIT.nano's facilities.

29

30

1 **References**

- 2
3
4 [1] *bp Statistical Review of World Energy 2020*, B. p.l.c **2021**.
- 5 [2] W. H. Wisler, *Energy Resources: Occurrence, Production, Conversion, Use*, Springer
6 New York, **1999**.
- 7 [3] a) T. Mattila-Sandholm, G. Wirtanen, *Food Rev. Int.* **1992**, 8, 573; b) A. Haryanto, S.
8 Fernando, N. Murali, S. Adhikari, *Energy & Fuels* **2005**, 19, 2098; c) T. Humplik, J. Lee, S.
9 C. O'Hern, B. A. Fellman, M. A. Baig, S. F. Hassan, M. A. Atieh, F. Rahman, T. Laoui, R.
10 Karnik, E. N. Wang, *Nanotechnology* **2011**, 22, 292001; d) J. D. Hansen, J. A. Johnson, D. A.
11 Winter, *Int. J. Pest Manage.* **2011**, 57, 267; e) J. Yang, X. Zhang, H. Qu, Z. G. Yu, Y. Zhang,
12 T. J. Eey, Y.-W. Zhang, S. C. Tan, *Adv. Mater.* **2020**, 32, 2002936; f) D. K. Nandakumar, Y.
13 Zhang, S. K. Ravi, N. Guo, C. Zhang, S. C. Tan, *Adv. Mater.* **2019**, 31, 1806730.
- 14 [4] a) A. Royne, C. J. Dey, D. R. Mills, *Sol. Energy Mater. Sol. Cells* **2005**, 86, 451; b) Y.
15 Liu, Y. Zhu, Y. Cui, *Nature Energy* **2019**, 4, 540; c) K. Ebrahimi, G. F. Jones, A. S. Fleischer,
16 *Renewable and Sustainable Energy Reviews* **2014**, 31, 622; d) L. L. Vasiliev, *Appl. Therm.*
17 *Eng.* **2005**, 25, 1.
- 18 [5] a) N. E. Todreas, M. S. Kazimi, *Nuclear Systems Volume I: Thermal Hydraulic*
19 *Fundamentals, Third Edition*, CRC Press, **2021**; b) J. Buongiorno, *Ann. Nucl. Energy* **2014**,
20 63, 9.
- 21 [6] a) L. Cheng, D. Mewes, A. Luke, *Int. J. Heat Mass Transfer* **2007**, 50, 2744; b) H. J.
22 Cho, D. J. Preston, Y. Zhu, E. N. Wang, *Nat. Rev. Mater.* **2016**, 2, 16092.
- 23 [7] a) K.-H. Chu, R. Enright, E. N. Wang, *Appl. Phys. Lett.* **2012**, 100, 241603; b) M. M.
24 Rahman, E. Ölçeroğlu, M. McCarthy, *Langmuir* **2014**, 30, 11225; c) N. S. Dhillon, J.
25 Buongiorno, K. K. Varanasi, *Nat. Commun.* **2015**, 6, 8247; d) R. Chen, M.-C. Lu, V.
26 Srinivasan, Z. Wang, H. H. Cho, A. Majumdar, *Nano Lett.* **2009**, 9, 548; e) H. Zhao, S. Dash,
27 N. S. Dhillon, S. Kim, B. Lettiere, K. K. Varanasi, A. J. Hart, *ACS Applied Nano Materials*
28 **2019**, 2, 5538.
- 29 [8] Y. Song, L. Zhang, C. D. Díaz-Marín, S. S. Cruz, E. N. Wang, *Int. J. Heat Mass*
30 *Transfer* **2021**, 122189.
- 31 [9] a) Y. Liu, J. Tang, L. Li, Y. N. Shek, D. Xu, *Int. J. Heat Mass Transfer* **2019**, 132, 25;
32 b) C. K. Yu, D. C. Lu, T. C. Cheng, *J. Micromech. Microeng.* **2006**, 16, 2092.
- 33 [10] Y. Song, S. Gong, G. Vaartstra, E. N. Wang, *ACS Appl. Mater. Interfaces* **2021**, 13,
34 12629.
- 35 [11] a) C. M. Patil, S. G. Kandlikar, *Int. J. Heat Mass Transfer* **2014**, 79, 816; b) A.
36 Jaikumar, S. G. Kandlikar, *Int. J. Heat Mass Transfer* **2016**, 95, 795; c) A. Jaikumar, S. G.
37 Kandlikar, *Appl. Phys. Lett.* **2016**, 108, 041604; d) S. Zhang, X. Jiang, Y. Li, G. Chen, Y.
38 Sun, Y. Tang, C. Pan, *Energy Convers. Manage.* **2020**, 209, 112665; e) J. Li, G. Zhu, D.
39 Kang, W. Fu, Y. Zhao, N. Miljkovic, *Adv. Funct. Mater.* **2021**, 31, 2006249; f) J. Li, W. Fu,
40 B. Zhang, G. Zhu, N. Miljkovic, *ACS Nano* **2019**, 13, 14080.
- 41 [12] Y. Song, H. Cha, Z. Liu, J. H. Seong, L. Zhang, D. J. Preston, E. N. Wang, *Int. J. Heat*
42 *Mass Transfer* **2021**, 122320.
- 43 [13] a) Y. Y. Hsu, *J. Heat Transfer* **1962**, 84, 207; b) P. Griffith, J. D. Wallis, *Chemical*
44 *Engineering Progress Symposium Series* **1958**, 56, 49.
- 45 [14] M. M. Rahman, J. Pollack, M. McCarthy, *Sci. Rep.* **2015**, 5, 13145.
- 46 [15] Y. Nam, S. Sharratt, C. Byon, S. J. Kim, Y. S. Ju, *Journal of Microelectromechanical*
47 *Systems* **2010**, 19, 581.

- 1 [16] a) Y. Im, C. Dietz, S. S. Lee, Y. Joshi, *Nanoscale Microscale Thermophys. Eng.* **2012**,
2 *16*, 145; b) K.-H. Chu, Y. S. Joung, R. Enright, C. R. Buie, E. N. Wang, *Appl. Phys. Lett.*
3 **2013**, *102*, 151602; c) M. M. Rahman, M. McCarthy, *J. Heat Transfer* **2017**, 139.
- 4 [17] Y. Song, L. Zhang, Z. Liu, D. J. Preston, E. N. Wang, *Appl. Phys. Lett.* **2020**, *116*,
5 253702.
- 6 [18] A. Jaikumar, S. G. Kandlikar, *Appl. Phys. Lett.* **2017**, *110*, 094107.
- 7 [19] a) J. Costa-Greger, A. Tsubaki, J. Gerdes, M. Anderson, C. Zuhlke, D. Alexander, J.
8 Shield, G. Gogos, presented at *2020 19th IEEE Intersociety Conference on Thermal and*
9 *Thermomechanical Phenomena in Electronic Systems (ITherm)*, 21-23 July 2020, **2020**; b) C.
10 Kruse, A. Tsubaki, C. Zuhlke, D. Alexander, M. Anderson, E. Peng, J. Shield, S. Ndao, G.
11 Gogos, *J. Heat Transfer* **2019**, 141.
- 12 [20] S. H. Kim, G. C. Lee, J. Y. Kang, K. Moriyama, M. H. Kim, H. S. Park, *Int. J. Heat*
13 *Mass Transfer* **2015**, *91*, 1140.
- 14 [21] K.-H. Chu, Y. Soo Joung, R. Enright, C. R. Buie, E. N. Wang, *Appl. Phys. Lett.* **2013**,
15 *102*, 151602.
- 16 [22] a) B. S. Kim, S. Shin, D. Lee, G. Choi, H. Lee, K. M. Kim, H. H. Cho, *Int. J. Heat*
17 *Mass Transfer* **2014**, *70*, 23; b) M.-C. Lu, R. Chen, V. Srinivasan, V. P. Carey, A. Majumdar,
18 *Int. J. Heat Mass Transfer* **2011**, *54*, 5359; c) Z. Yao, Y. W. Lu, S. G. Kandlikar, *Int. J.*
19 *Therm. Sci.* **2011**, *50*, 2084.
- 20 [23] D. E. Kim, S. C. Park, D. I. Yu, M. H. Kim, H. S. Ahn, *Appl. Phys. Lett.* **2015**, *107*,
21 023903.
- 22 [24] A. Zou, S. C. Maroo, *Appl. Phys. Lett.* **2013**, *103*, 221602.
- 23 [25] H. Kim, H. S. Ahn, H. J. Kwak, M. H. Kim, D. E. Kim, *Appl. Phys. Lett.* **2016**, *109*,
24 243901.
- 25 [26] Y. Song, C. Wang, D. J. Preston, G. Su, M. M. Rahman, H. Cha, J. H. Seong, B.
26 Philips, M. Bucci, E. N. Wang, *ACS Appl. Mater. Interfaces* **2022**, *14*, 9788.
- 27 [27] a) J. K. Lee, A. Bazylak, *Joule* **2021**, *5*, 19; b) J. K. Lee, C. Lee, K. F. Fahy, B. Zhao,
28 J. M. LaManna, E. Baltic, D. L. Jacobson, D. S. Hussey, A. Bazylak, *Cell Reports Physical*
29 *Science* **2020**, *1*, 100147; c) R. Iwata, L. Zhang, K. L. Wilke, S. Gong, M. He, B. M. Gallant,
30 E. N. Wang, *Joule* **2021**, *5*, 887; d) L. Yang, L. Loh, D. K. Nandakumar, W. Lu, M. Gao, X.
31 L. C. Wee, K. Zeng, M. Bosman, S. C. Tan, *Adv. Mater.* **2020**, *32*, 2000971; e) J. R. Lake, Á.
32 M. Soto, K. K. Varanasi, *Langmuir* **2022**, *38*, 3276.
- 33